

Mercaptosilane Engineered Interface with Surface-Preferred Crystal Plane for High-Performance Zn Anode

Guo-Xian Li,^{*[a]} Zhen Zhao,^[a] Wei Yu,^[a] Chui-Zhou Meng,^{*[a]} and Shi-Jie Guo^[a]

Zn-ion battery (ZIB) has drawn huge attentions as a prospective energy storage system for the next generation, but dendrite and side reaction issues related to Zn have limited their potential applications. Here, a combined approach involving the modification of surface texture and the implementation of a passivation layer is proposed to tackle the problem. A zinc-silane composite layer is coated on (002)-preferred Zn (ZSi@Zn) by selective acid etching, concomitant with the hydrolysis of Mercaptosilane. The preferred (002) crystal plane, in conjunction with the zinc-silane composite layer, leads in integrated

interfacial transport and deposition control. As a result, the ZSi@Zn electrode has dramatically increased stability and uniform Zn deposition behavior. Remarkably, it exhibits a Coulombic efficiency of approximately 99.4%, a long lifespan of around 3000 hours at the current density of 1 mA cm^{-2} with a capacity of 0.5 mAh cm^{-2} . The excellent reversibility of zinc persists with current densities of 2, 5, and 10 mA cm^{-2} . Furthermore, Zn-MnO₂ battery constructed with ZSi@Zn also delivers excellent performance, manifesting a capacity retention of 88.4% after 4000 cycles.

Introduction

Zn-ion batteries have recently gained huge attention as a compelling solution for environmentally friendly electrochemical energy storage.^[1] However, the implement of Zn anodes is impeded by challenges such as dendrite growth and side reactions. The unevenness of commercial Zn foil, characterized by protrusions, promotes dendrite growth and non-uniform nucleation, ultimately lead to compromised cyclic stability and accelerated battery failure.^[2] Additionally, thermodynamic instability of Zn in electrolytes results in electrochemical corrosion, which produces insulating byproducts and consumes electrolytes, further contributing to a significant deterioration of electrochemical performance.^[3]

Considering that the challenges associated with dendrite growth and electrochemical corrosion of Zn are intricately linked to the interface between electrode and electrolyte, meticulous control and effective management of this interface are imperative to guarantee the high performance of Zn anode.^[4] A lot of methods have been employed to establish stable electrode-electrolyte interfaces, such as the construction of 3D electrode structures,^[5] electrolytes designing,^[6] modification of Zn surface,^[7] and regulating of separators,^[8] etc. Among these approaches, surface modification has arisen as a straightforward and efficient strategy to address the aforementioned

issues. A range of materials (e.g., carbon-based materials,^[9] metal oxides,^[10] MXene,^[11] metal alloys,^[12] inorganic salts,^[13] metal sulfides,^[14] metal fluoride,^[15] ferroelectric materials,^[16] MOF-based materials^[17]) have been coated onto Zn foils as artificial interfacial layers. These coatings have proven effective in enhancing the stability of zinc anodes. Different techniques for surface modification have been developed to achieve this goal, such as slurry coating,^[18] wet chemistry,^[19] atomic layer deposition,^[20] chemical vapor deposition,^[21] as well as ion beam sputtering.^[22] Of these methods, wet chemistry stands out as an easy and scalable approach, and as such, has been widely adopted in the modification of Zn substrates. Regrettably, the use of passivation layers may bring about an increase in interfacial resistance and nucleation overpotential when plating and stripping, ultimately hampering the implement of ZIBs by deteriorating their rate performance.

It is preferable to promote lateral growth of Zn. So, the manipulation of the crystal orientation of Zn metal has been employed to enhance the performance of Zn anodes.^[23] For example, Zhou et al.^[24] found that Zn metal anodes with preferred (002) crystal plane are superior over that of (100) plane in terms of less dendrites, low hydrogen evolution, and minimal byproducts. This is because there is a more even arrangement of Zn atoms and charge density on (002) plane, leading to the uniform flux of Zn²⁺ ions. Based on the differences in atomic binding energy and surface energy of different crystal surfaces, acid etching shows its ability to selectively remove (100) planes while preserving (002) planes. Wang et al.^[25] discovered that phosphoric acid provides a etching effect on Zn surface, resulting in the exposure of more (002) planes. Su et al.^[26] subjected Zn to concentrated phosphoric acid treatment, resulting in a striped Zn array with a preference of (002) plane. While the Zn (002) texture proves advantageous in facilitating smooth deposition, the direct interaction between metallic zinc and corrosive electrolytes inevitably leads to side reactions. Consequently, the ability to

[a] Dr. G.-X. Li, Z. Zhao, Dr. W. Yu, Prof. Dr. C.-Z. Meng, Prof. Dr. S.-J. Guo
State Key Laboratory for Reliability and Intelligence of Electrical Equipment;
Hebei Key Laboratory of Smart Sensing and Human-Robot Interaction;
Engineering Research Center of the Ministry of Education for Intelligent
Rehabilitation Equipment and Detection Technologies;
School of Mechanical Engineering, Hebei University of Technology,
No. 5340, Xiping Road, Beichen District, Tianjin 300401, China
E-mail: gxli@hebut.edu.cn
2018108@hebut.edu.cn

 Supporting information for this article is available on the WWW under
<https://doi.org/10.1002/batt.202300544>

reverse zinc plating/stripping is compromised, especially over prolonged cycles. So, it becomes essential to harness the cooperative interaction between the Zn(002) texture and the passivation layer. Zhang et al.^[27] elevated the Zn(002) exposure on the anode's surface, while simultaneously creating an amorphous borate layer through a hydrothermal process involving boric acid. Song et al.^[28] used a general annealing approach to coat passivation layers on the Zn anodes, which led to the simultaneous realization of (002) plane preferred surface and the formation of zinc compounds. Furthermore, they explored the synergistic impact arising from the combination of the (002) plane and surface coating. Although significant progress has been made in modifying Zn through these methods, developing an affordable and scalable approach for a (002) preferred Zn with a protection layer remains a challenge.

Organosiloxane is widely utilized to safeguard metal surface. Through hydrolysis and polycondensation, organosiloxane can form coatings that have the properties of both organic and inorganic polymers. In this investigation, we introduce a straightforward surface modification approach involving the hydrolysis reaction of (3-Mercaptopropyl trimethoxysilane (MPTMS) at pH=4. This process yields a zinc-silane composite layer on the acid-etching induced (002)-preferred Zn. The zinc-silane composite layer in turn form a robust interaction with Zn through Si–O–Zn, establishing a robust interface between the modifying layer and Zn foil.^[29] The strong zinc-affine groups and molecular nanochannels have been documented to assist the homogeneous deposition of zinc, while thiol molecules have shown a preference for binding to the less stable zinc crystal facets through robust Zn–S bonding interactions.^[30] In the meantime, zinc compounds have been documented to possess potent Zn²⁺ adsorption capabilities, which can improve ion kinetics and promote uniform Zn plating and stripping.^[31] Meanwhile, the (002) plane can encourage the lateral growth of Zn metal, resisting the corrosion of the electrolyte and suppressing the growth of Zn dendrites. Due to the synergistic effects of these attributes, both the symmetrical cells and the corresponding full batteries exhibit markedly improved stability.

Methods

Preparation of ZSi@Zn

MPTES, water and ethanol were mixed in a ratio of 6:4:90. Acetic acid was used to regulate the pH of the solution to about 4. A Zn foil of 100 μm thickness was then immersed in the solution for varying lengths of time (ranging from 0.5 to 4 hours). Following the ethanol rinsing and drying at room temperature, the zinc-silane composite layer was generated on the Zn foil through thermal treatment at 100 °C for 1 hour. The bare Zn foil and treated Zn foil were punched into discs (Φ12 mm) for direct use as Zn anodes. The as-obtained foils are denoted as ZSi@Zn-xh, with x representing immersing time. If not otherwise specified, ZSi@Zn is equivalent to ZSi@Zn-2h. HAc@Zn and Si@Zn were prepared using a similar protocol as for ZSi@Zn without MPTES and acetic acid, respectively.

Preparation of α-MnO₂ cathode

A hydrothermal method was used to prepare α-MnO₂ according to literature.^[32] Typically, 0.05 g of polyvinylpyrrolidone (PVP) was mixed with 40 mL of 0.015 M KMnO₄ solution. The resulting solution was then poured into a 50 mL Teflon-lined autoclave. The autoclave was held at 160 °C for a duration of 10 hours, after which it was allowed to cool naturally to room temperature. The precipitates were obtained through filtration, and then washed repeatedly with distilled water and absolute ethanol. The solid was dried at 60 °C for 8 hours, and the resulting α-MnO₂ nanowires were obtained by calcination at 300 °C for 10 hours. Subsequently, 50 mg α-MnO₂ and 25 mg SWCNT were introduced into a 12.5 g aqueous dispersion that included 250 mg sodium cholate. The blend underwent ultrasonication for 2 hours using a horn-type ultrasonic probe. Subsequently, the blended solution underwent filtration and multiple rinses with deionized water before being dried at 60 °C. The achieved effective mass loading of MnO₂ is approximately 2.0–3.0 mg cm⁻².

Materials Characterizations

Morphological characterization was conducted with scanning electron microscopy (SEM) on a TESCAN GAIA3 instrument. X-ray photoelectron spectrometer (XPS) analyses were carried out using an ESCALAB Xi+ (Thermo Fisher Scientific, Al Kα radiation, $h\nu = 1486.6$ eV). The in-situ optical photographs were taken by a metallurgical microscope (VIYEE, WY-2000M). X-ray diffraction (XRD) detections were conducted using a Bruker D8 advanced diffractometer (Cu Kα radiation, $\lambda = 0.154$ nm) with a scan rate of 10° min⁻¹. The component content was determined using thermogravimetric analysis (TGA, Mettler TGA/DSC1).

Electrochemical Measurements

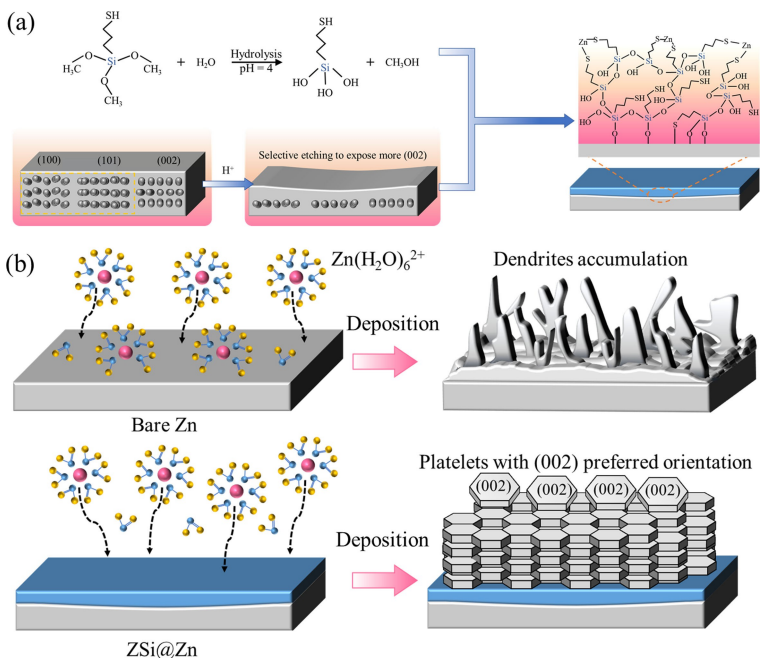
Electrochemical performances of the ZSi@Zn and bare Zn were evaluated at room temperature using CR2032 coin cells, with 2M ZnSO₄ electrolyte and glass fiber (GF/A, whatman) separator. Each coin cell was supplied with 80 μL of electrolytes. Symmetric cells were constructed to assess the stability of Zn plating/stripping processes, employing fixed current density and Zn capacity.

Zn//Cu asymmetric cells were utilized to evaluate the Coulombic efficiency (CE) of Zn anode. The tests involved plating Zn onto the Cu electrodes at a fixed current density and fixed Zn capacity, followed by stripping the plated Zn from the Cu electrodes using the same current density. A voltage limit of 0.5 V was applied during the stripping process. CEs were assessed by computing the ratios of Zn stripping to plating capacities.

For ZSi@Zn//MnO₂ batteries, the α-MnO₂/SWCNT films were used as the cathode, with 2M ZnSO₄+0.2M MnSO₄ electrolyte and glass fiber (GF/A, whatman) separator. Specific capacity and current density were calculated according to the mass of active material. The ZSi@Zn//MnO₂ batteries were evaluated within a voltage range of 0.5–2.0 V. NETWARE battery test system were used for galvanostatic discharge/charge (GCD) tests. Cyclic voltammetry (CV) tests, electrochemical impedance spectroscopy (EIS, 10 mHz to 100 kHz) measurements, and chronoamperometry (CA) were evaluated using an Correst workstation.

Results and discussion

The preparation process of ZSi@Zn is shown in Scheme 1. After inserting the zinc foil into a MPTES-containing solution with



Scheme 1. (a) Proposed reactions for the preparation of ZSi@Zn. (b) Mechanism comparison of the deposition pathways for bare Zn and ZSi@Zn.

pH=4, a zinc compound is produced by acid etching of the Zn foil, which result in a (002) preferred plane orientation of Zn. The MPTES-containing solution treatment without acid had no significant effect on the crystal plane orientation of Zn (Figure S1). Accompanied by acid etching, MPTES undergoes hydrolysis, condenses with zinc compounds, and ultimately bonds to the Zn foils, creating a composite layer. The color of Zn foils coated with the zinc-silane composite layer becomes white after the synthesis (Figure S2). The electrode interface is very important in distributing the surface charges and regulating the movement of ions and electrons. Figure 1a, b and Figure S3 display the SEM images of bare Zn, HAc@Zn, Si@Zn and ZSi@Zn. Notably, the surface of bare Zn exhibits numerous scratches (Figure 2a). After acid treatment, the surface of the Zn

foil becomes uneven with sidestep-like structure due to the selective etch on Zn. While Si@Zn shows a smooth surface. ZSi@Zn exhibits a nanostructured surface (Figure 2b), which probably caused by the selective corrosion of (001) planes. The nanostructured surface may promote uniform distribution of the electric field and uniform nucleation and plating of zinc.^[33] The thickness of the coating is about ~500 nm (Figure 1c). We also explored the optimal treatment duration for Zn. A brief treatment duration does not guarantee the production of a uniform layer. Figure S4 illustrates that numerous small nanoparticles can be detected on ZSi@Zn. In contrast, in Figure S4c, a substantial amount of deposition is evident on the Zn surface with the extension of the treatment duration to 4 hours. The optimal processing time is selected to be 2 h. EDS analysis

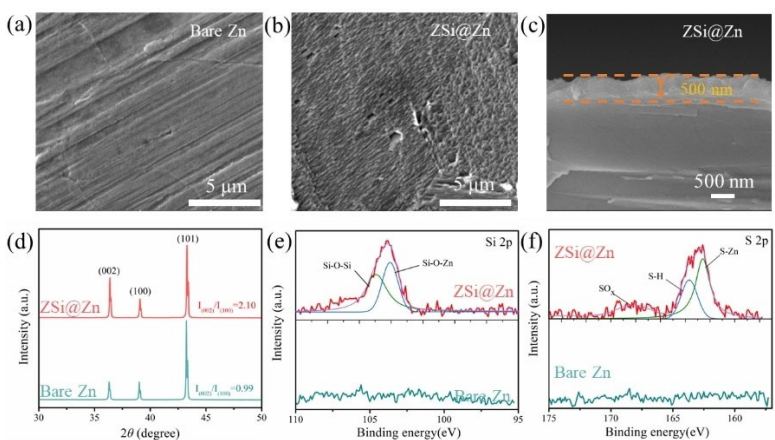


Figure 1. SEM images of the (a) Bare Zn, (b) ZSi@Zn. (c) side-view SEM image of ZSi@Zn. (d) XRD patterns and $I_{(002)}/I_{(100)}$ of the Bare Zn and ZSi@Zn. XPS spectra of (e) Si 2p and (f) S 2p on bare Zn and ZSi@Zn.

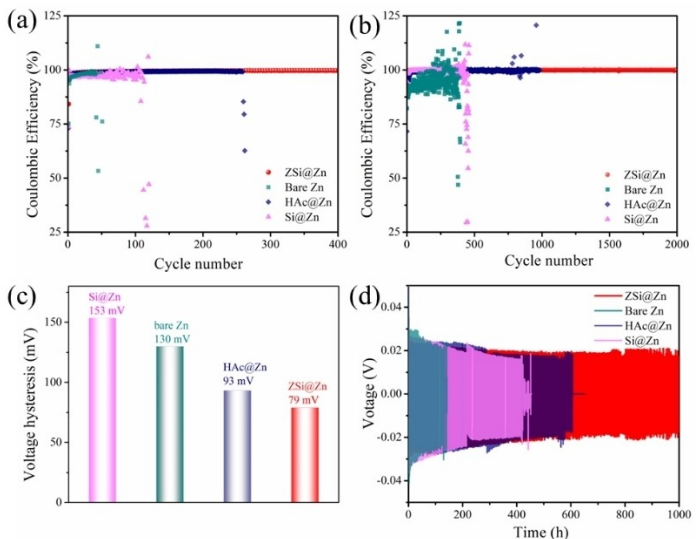


Figure 2. Electrochemical characteristics of ZSi@Zn, HAc@Zn, Si@Zn, and Bare Zn. CEs of the Zn//Cu cells at (a) 1 mA cm^{-2} and (b) 10 mA cm^{-2} with a Zn deposition capacity of 1 mAh cm^{-2} and (c) voltage hysteresis of the Zn//Cu asymmetric cells; (d) cycling performance of the Zn//Zn cells at a current density of 1 mA cm^{-2} for 1 mAh cm^{-2} .

confirms a evenly distributed of O, Si, S, and Zn elements. (Figure S5), identifying the formation of homogenous zinc-silane composite layer.

XRD patterns for bare Zn and ZSi@Zn were tested and are presented in Figure 1d and Figure S6. The bare Zn sample showed peaks at 36° , 38° , and 43° , agreeing with the characteristic peaks of (002), (100), and (101) planes for crystalline Zn (JCPDS No. 04-0831). The relative intensities of (002) to (100) diffractions were significantly higher in the ZSi@Zn sample compared to the bare Zn sample after surface modification. Immersing Zn into a MPTES-containing solution with $\text{pH}=4$ resulted in an increase in $I_{(002)}/I_{(100)}$ from 0.99 (Bare Zn) to 2.10 (ZSi@Zn), indicating that the selective etching reaction had occurred.^[26]

To explore the chemical surroundings of the coated layer, XPS measurements were performed. The formation of Si–O–Zn in ZSi@Zn is evidenced by the existence of Si 2p on ZSi@Zn, which displays a pronounced and broad Si–O peak. This peak can be deconvoluted into Si–O–Si (101.03 eV) and Si–O–Zn (101.9 eV). The S 1s spectrum of ZSi@Zn reveals three peaks at 162.3, 163.5, and 168.5 eV (Figure 1f), consistent with S–Zn, S–H, and oxidized SO_x species (sulfinate and sulfonates).^[29a,34] In contrast, bare Zn exhibits no discernible peaks.

Bare Zn, HAc@Zn, and Si@Zn were used as controls to gain insights into the synergy between zinc-silane composite layer (ZSi) and (002)-textured Zn. Zn foils with preferential Zn(002) crystal plane were obtained by acetic acid treatment. Figure 2a shows the cycling performance of ZSi@Zn//Cu asymmetric cell with an average CE of about 99.5% throughout 400 cycles at 1 mA cm^{-2} , deposited capacity of 1 mAh cm^{-2} and a voltage upper-limit of 0.5 V, demonstrating the excellent reversibility of zinc plating/stripping. However, the cycling life of the bare Zn//Cu asymmetric cell last only 41 cycles, exhibiting significant rises and falls in CE, likely due to side reactions and the growth

of zinc dendrites. The synergistic impact of the Zn(002) texture and surface coating was evaluated through comparative tests of Si@Zn//Cu and HAc@Zn//Cu asymmetric cells. Their cycling lifespans exceed that of pure Zn but fall short of ZSi@Zn. These findings suggest that both surface coating and Zn(002) can improve electrochemical performance. However, neither surface coating nor Zn(002) in isolation can significantly boost electrochemical performance. The exceptional performance of ZSi@Zn is also apparent at the cell cycled at 10 mA cm^{-2} (Figure 2b). Figure S7 shows GCD curves of the cells at 10 mA cm^{-2} , where the Zn//Cu cell with ZSi@Zn has a voltage hysteresis of 79 mV (Figure 2c), lower than those of bare Zn (130 mV), HAc@Zn (93 mV), and Si@Zn (153 mV), suggesting a significant enhancement in the uniformity of zinc electrodeposition when assembled with ZSi@Zn. In symmetric cells, ZSi@Zn demonstrates remarkable stability for over 1000 hours, as illustrated in Figures 2d. This stability surpasses that of bare Zn, HAc@Zn, and Si@Zn. The outcome reaffirms the superior qualities of ZSi@Zn, aligning with the conclusions drawn from the asymmetric cells. In summary, the combined effect of Zn(002) and surface coating effectively suppresses parasite reactions, prolongs cycling durability, and reduces overpotential.

Having successfully formed the ZSi layer, we proceeded to elucidate its benefits in improving anode kinetics. Due to the modified surface, ZSi@Zn demonstrates enhanced wettability with the electrolyte, as depicted in Figure 3a, b. The contact angle with 2 M ZnSO_4 solution decreases from 98° (bare Zn) to 75° (ZSi@Zn), which contributes to a reduction in charge transfer resistance. The presence of the hydrophobic alkyl group in MPTES results in an increased contact angle of Si@Zn with a 2M ZnSO_4 solution, reaching 113° . While the contact angle of HAc@Zn with 2M ZnSO_4 solution decreases to 65° , arising from the hydrophilic surface and uneven morphology related to acid treatment (Figure S8).

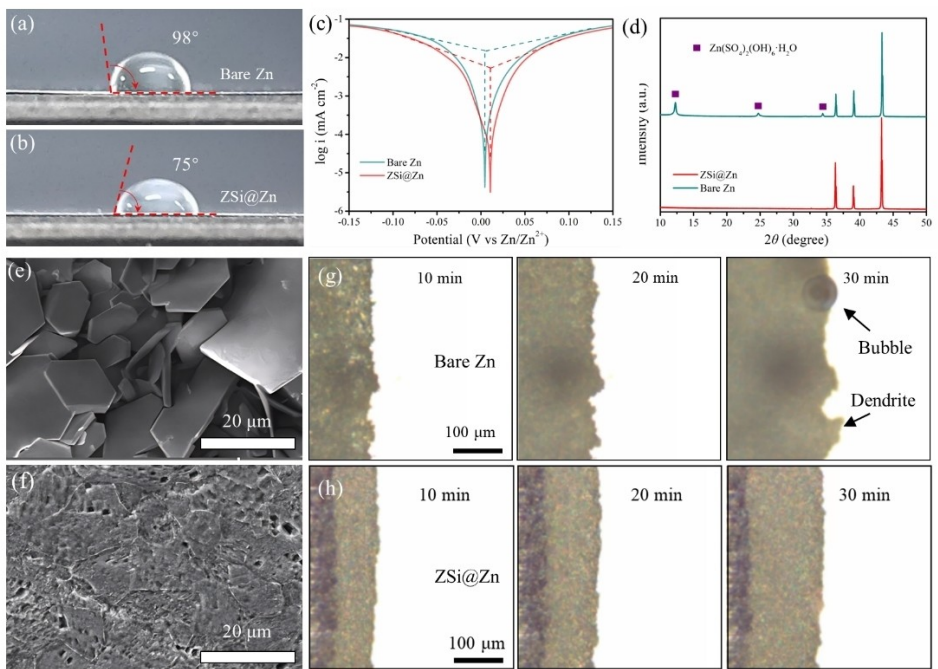


Figure 3. Contact angles of the 2 M ZnSO_4 electrolyte on (a)bare Zn and (b) ZSi@Zn. (c) Linear polarization plots of bare Zn and ZSi@Zn. (d) XRD patterns of bare Zn and ZSi@Zn after immersion in the electrolyte for a period of 7 days and the respective SEM images of (e) bare Zn and (f) ZSi@Zn. In situ optical microscope observation of the Zn deposition process with (g) bare Zn and (h)ZSi@Zn.

The zinc-silane composite layer's enhanced wettability is anticipated to regulate Zn plating and minimize side reactions. The CV curves for deposition and stripping of Zn and ZSi@Zn on Cu were obtained and presented in Figure S9. These curves display a solitary oxidation peak during zinc deposition and a corresponding reduction peak during zinc stripping, affirming the electrochemical stability of the deposited layer. The nucleation overpotential in the CV curves is 73 mV for ZSi@Zn, while the corresponding nucleation overpotential of bare Zn is 90 mV, indicating the boosted charger transfer kinetics. In addition, the Zn//Cu cell with ZSi@Zn exhibits higher current intensity than the bare Zn. This suggests an augmentation in nucleation sites, thereby promoting rapid and uniform deposition of Zn. Because anions migrate faster than solvated Zn^{2+} ions, the Zn^{2+} transference number for bare Zn is 0.22 (as illustrated in Figure S10a), aligning with previous reports.^[35] The transfer number of Zn^{2+} can be increased to 0.58 in Zn//Zn cell featuring ZSi@Zn anode, as shown in Figure S10b. This enhancement can be attributed to the interactions of zinc-silane composite layer with Zn^{2+} , which changes the ion transport behavior.^[14,23a] These improvements are beneficial for mitigating concentration polarization and ensuring a uniform distribution of Zn^{2+} during the Zn stripping/plating process of the anode. In Figure S11, a comparison is made between the nucleation potential and plateau overpotentials of bare Zn electrodes and ZSi@Zn (1 mA cm^{-2} and 1 mAh cm^{-2}). By incorporating a zinc-silane composite layer, the nucleation potential was significantly reduced from 56.2 mV to 22.9 mV, and the plateau overpotentials decreased from 25.6 mV to 16.8 mV, suggesting a reduced energy barrier for the deposition of zinc.^[18a] This suggests that the zinc-silane composite layer

promotes the generation of crystal nuclei and enhances the transfer rate of Zn^{2+} .

The resistance of ZSi@Zn against electrolyte-induced corrosion was examined through linear polarization tests conducted on Zn//Zn symmetric cells. Figure 3c illustrates that the anode exhibits enhanced electrochemical stability against corrosion in the electrolyte, as evidenced by a higher corrosion potential (increased from 0.016 to 0.032 V) and a lower corrosion current (decreased from $2.63 \text{ to } 0.71 \text{ mA cm}^{-2}$) when protected by zinc-silane composite layer.

The cycling of Zn is accompanied by a detrimental parasitic reaction of H_2 evolution, which leads to an increase in local alkalinity at the interface between the Zn and electrolyte, ultimately resulting in water-induced corrosion and the generation of unwanted by-products. To assess protective efficacy of the zinc-silane composite layer, we directly immersed both bare zinc and ZSi@Zn in ZnSO_4 electrolyte for one week. In bare zinc anodes, discernible peaks were observed, indicative of $\text{Zn}_4\text{SO}_4(\text{OH})_6 \cdot \text{H}_2\text{O}$ formation (JCPDS No. 39-0690) (Figure 3d). SEM images of the bare Zn after immersion revealed the presence of numerous large flakes (Figure 3e). Conversely, the immersed ZSi@Zn exhibited a clean surface with fewer by-products, consistent with XRD data (Figure 3f). The immersed Si@Zn displayed a pristine surface due to its hydrophobic surface. In contrast, the SEM image of HAc@Zn after immersion treatment revealed the presence of numerous nanoflakes (Figure S12). These findings confirm the zinc-silane composite layer's capacity to safeguard the Zn anode against electrolyte corrosion and reduce side reactions. The linear sweep voltammetry (LSV) curves were conducted in Na_2SO_4 aqueous solution to further estimate the ability of the zinc-silane composite layer

to suppress H₂ evolution. It can observe that ZSi@Zn displays lower current density than bare Zn across the entire sweep, suggesting reduced H₂ generation on ZSi@Zn (Figure S13). Furthermore, ZSi@Zn exhibits a more negative onset potential (-1.43 V), suggesting a superior capability to impede H₂ evolution. At a potential of -1.5 V, the response current of ZSi@Zn is significantly lower (0.2 mA cm^{-2}) compared to bare Zn (2.5 mA cm^{-2}), which confirms reduced H₂ generation on ZSi@Zn.

The electrochemical surface area (ECSA) was measured and presented in Figure S14. Figure S14a, b shows cyclic voltammetry curves in the non-Faraday region, acquired with $1\text{ M Na}_2\text{SO}_4$ as the electrolyte at varying scan rates ($20\text{--}100\text{ mV s}^{-1}$). The fitting process was used to calculate the double-layer capacitance (Cdl), and the results are presented in Figure S14c, d. The bare Zn has an ECSA of 3.67 cm^2 . The coating of zinc-silane composite layer on Zn reduces the ECSA to 0.08 cm^2 , suggesting the development of a compact and corrosion-resistant layer. The reduced ECSA of ZSi@Zn indicates a lower anode surface activity, which inhibits Zn corrosion and the HER process.^[19b]

In-situ optical microscopy was used to monitor the morphological variations while undergoing zinc deposition process on bare Zn and ZSi@Zn. Following a 10-minute plating duration, the surface of the bare Zn became uneven, with observable protrusions. Subsequently, noticeable Zn dendrites emerged along with gas bubbles, indicating uneven Zn plating on bare Zn and the presence of parasite reactions (Figure 3g, h). In contrast, there was no growth of dendrites on ZSi@Zn and the consistency of the Zn plating was maintained. This clearly illustrates the substantial influence of the zinc-silane composite layer and the (002) texture in regulating the zinc plating procedure. To study the evolution of cathode and anode morphology in Zn//Zn symmetric batteries, we collected ex-situ SEM images of the electrodes following the plating of 1 mAh cm^{-2} Zn at 1 mA cm^{-2} (Figure S15). Previous research has highlighted that the first process in ZIBs is stripping, which can lead to the formation of inhomogeneous void spaces and severe dendrite problems.^[36] Our SEM images illustrate that ZSi@Zn results in a layer of zinc deposition that is uniform and densely packed, devoid of observable dendritic structures. In contrast, the bare Zn surface exhibits randomly distributed Zn, transforming into a three-dimensional porous configuration. The stripped bare Zn shows large pits due to nonuniform metal dissolution, while the stripped ZSi@Zn exhibits a relatively flat surface, indicating more uniform stripping of Zn.

To enhance our comprehension of the functionality of the ZSi@Zn, activation energy (Ea) was ascertained by Arrhenius equation, which characterizes the transfer processes of Zn ions.^[37] The charge transfer resistances (Rct) of Zn//Zn cells were assessed using EIS across temperatures ranging from 20 to 60°C (as shown in Figure 4a, b and Table S1). The activation energy for ZSi@Zn is lower at 11.73 kJ mol^{-1} compared to the bare Zn electrode at 26.21 kJ mol^{-1} (as illustrated in Figure 4c), which suggests that the zinc-silane composite layer enables faster Zn ion transport during Zn stripping/plating.

The deposition behavior of ZSi@Zn was further investigated using a CA test. The results show that, under an applied

overpotential of -150 mV, the ZSi@Zn electrode demonstrated a reduced 2D diffusion process and maintained a stable 3D diffusion process (Figure 4d).^[35,38] Normally, Zn ions tend to diffuse along the surface to minimize surface energy and migrate towards energetically favorable sites, such as tip sites or areas with defects. However, the zinc-silane composite layer contains numerous Zn²⁺ transport channels, which uniformly distribute the Zn²⁺ flux. Consequently, a consistent and continuous 3D accumulation of Zn can be achieved.

Rate performance tests were conducted on symmetrical cells with current densities ranging from 0.5 to 10 mA cm^{-2} , with a deposition/stripping capacity of 1.0 mAh cm^{-2} . The ZSi@Zn symmetrical cell has substantially lower and more stable voltage hysteresis across various current densities compared to the bare Zn symmetrical cell (Figure 4e, f). This suggests an improved electrochemical performance of the ZSi@Zn anode.

Symmetric Zn cells were subjected to galvanostatic cycling tests at different current densities and capacities to evaluate their cycling performance. The cycling stability of Zn and ZSi@Zn cells under a current density of 1 mA cm^{-2} and a capacity limitation of 0.5 mAh cm^{-2} is depicted in Figure 4g. Random voltage oscillations and subsequent failure occurred in the bare Zn//Zn cell at approximately 480 hours, which could be caused by short circuits originated from dendrites. On the contrary, the cell utilizing ZSi@Zn demonstrated stable polarization voltage and an exceptionally long cycling life of 3000 hours. Furthermore, when charged and discharged at current densities of 2 , 5 , and 10 mA cm^{-2} (Figure S16), the ZSi@Zn electrode showed significantly better cycling stability in comparison to the bare Zn electrode. The influence of varying thicknesses of Zn-silane layers on the stability of anodes was explored. Results indicate that the ZSi@Zn electrode obtained after 2 hours of treatment is the most effective in enhancing stability (Figure S17). ZSi@Zn with a treatment time of 1 h displayed a small over-potential and stability of 300 hours at 1 mA cm^{-2} for 1 mAh cm^{-2} . The use of a ZSi@Zn obtained after 4 hours of treatment resulted in a large over-potential and cycling life of about 520 hours, indicating that the thick layer hinders interface ionic diffusion. The morphology of the electrodes after 50 cycles at 1 mA cm^{-2} with 1 mAh cm^{-2} is depicted in the SEM images in Figure 4h, i. The particles deposited onto the bare Zn exhibit a non-uniform distribution comprising mossy-like deposits that are aggregates of zinc flakes, corrosion products, and glass fibers, whereas the ZSi@Zn showcases a dense and smooth surface devoid of dendrites. Post-cycling elemental analysis of ZSi@Zn reveals robust and well-aligned signals for Zn, Si, and C. (Figure S18). This provides evidence that the Zn-silane layer can sustain effective coverage after cycling. In addition, we examined the crystal structure of the Zn electrode as mentioned above by performing ex-situ XRD measurements. The Zn deposited ZSi@Zn showed a significantly stronger (002) diffraction peak compared to bare Zn and Zn deposited bare Zn. The intensity ratio between the (002) and (101) planes in the cycled ZSi@Zn is markedly increased in comparison to that of bare Zn (Figure 4j). This is likely due to the presence of in situ generated zinc compounds and the acid-

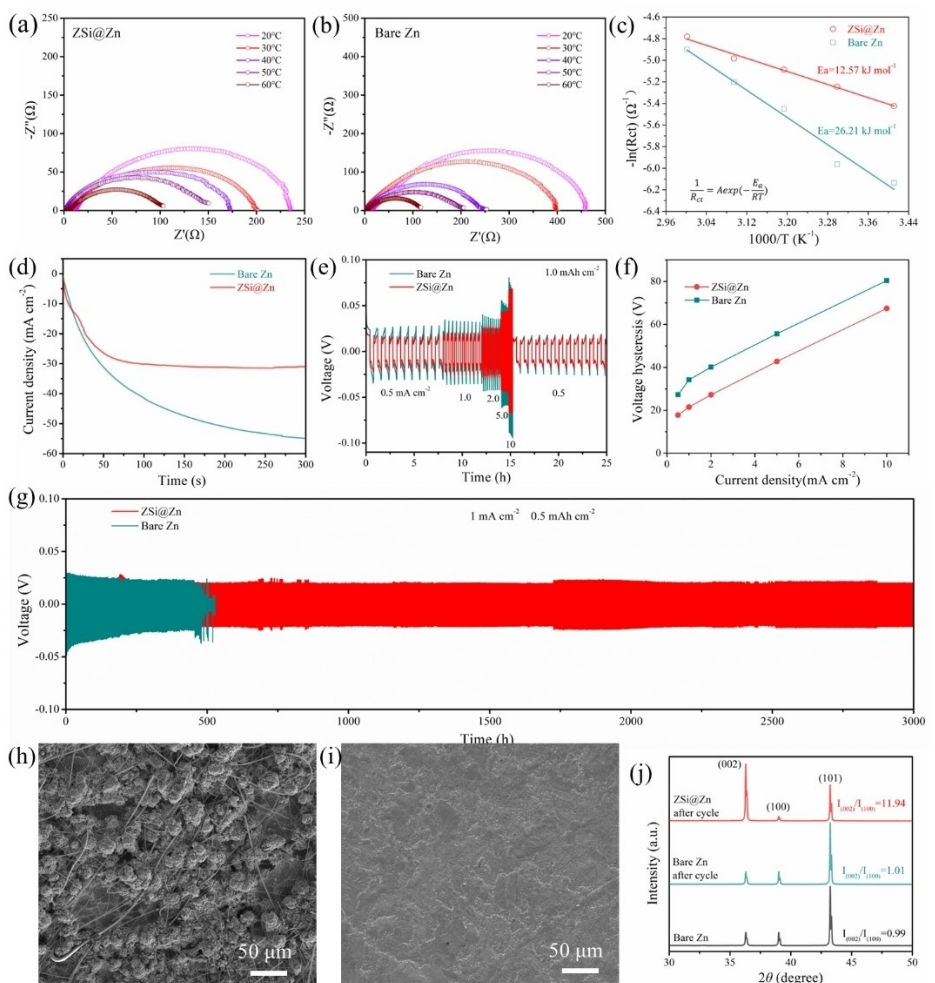


Figure 4. Nyquist curves of Zn//Zn cells with (a) bare Zn and (b) ZSi@Zn under different temperatures. (c) The corresponding Arrhenius plots. (d) CA curves of Zn and ZSi@Zn electrodes at a -150 mV overpotential. (e) Rate performance of the symmetric cells. (f) The voltage-hysteresis of symmetric cells with bare Zn or ZSi@Zn under different current densities of 0.5 to 10 mA cm^{-2} . (g) The cycling durability of symmetrical cells using bare Zn or ZSi@Zn as the electrodes at 1 mA cm^{-2} for 0.5 mAh cm^{-2} . SEM images of (h) bare Zn and (i) ZSi@Zn after 50 cycles at 1 mA cm^{-2} for 1 mAh cm^{-2} . (e) XRD patterns of initial Zn foil, bare Zn and ZSi@Zn after cycling.

etching induced (002) texture. They can enhance Zn^{2+} ion kinetics, control deposition/stripping behaviors, and lead to the preferential deposition along the Zn (002) plane. These encouraging outcomes underscore the efficacy of ZSi@Zn in suppressing dendrite growth, enhancing stability, and consequently, achieving higher Coulombic efficiencies and improved cycle life.

To investigate the potential applications of the ZSi@Zn electrode, batteries were assembled (Zn/MnO_2 and ZSi@Zn// MnO_2 , with 2M $\text{ZnSO}_4 + 0.2\text{M}$ MnSO_4 as electrolyte). The MnO_2 was synthesized using a hydrothermal method. The composition and morphology are consistent with the results reported in the literature^[32] (Figure S19). In order to enabling efficient utilization of the active materials for performance enhancement, the cathode was made of a freestanding and binder-free $\text{MnO}_2@\text{single-walled carbon nanotube (SWCNT)}$ film, which was obtained by filtration of a mixed dispersion of MnO_2 and SWCNT (see Experimental section). Based on the TGA result, the weight percentage of the electrochemical active

material $\alpha\text{-MnO}_2$ in the electrode was ca. 63% (Figure S20). Analysis of CV curves indicated that Zn/MnO_2 batteries with both bare Zn and ZSi@Zn anodes displayed comparable redox peaks, suggesting that they undergo the same electrochemical reactions (Figure 5a). Figure S21 depicts the GCD profiles of batteries under current densities varying from 0.5 to 5.0 Ag^{-1} . The cathode assembled with ZSi@Zn delivers 318, 256, 205, 158 and 145 mAh g^{-1} capacities at 0.5 , 1 , 2 , 3 and 5 Ag^{-1} , respectively. In comparison, the cathode assembled with bare Zn delivers 272, 224, 155, 134 and 114 mAh g^{-1} capacities at the corresponding current densities. The charge storage mechanism may be based on a hybrid storage mechanism including $\text{Mn}^{2+}/\text{MnO}_2$ deposition/dissolution, Zn^{2+} insertion, and chemical conversion, which need to be further explored.^[39] Figure 5b shows a comparison of the rate performance between Zn/MnO_2 batteries with bare Zn and ZSi@Zn anodes. Zn/MnO_2 battery with ZSi@Zn anode consistently exhibits higher specific capacities than the battery with bare Zn at different current densities. This disparity in rate capability can be attributed to

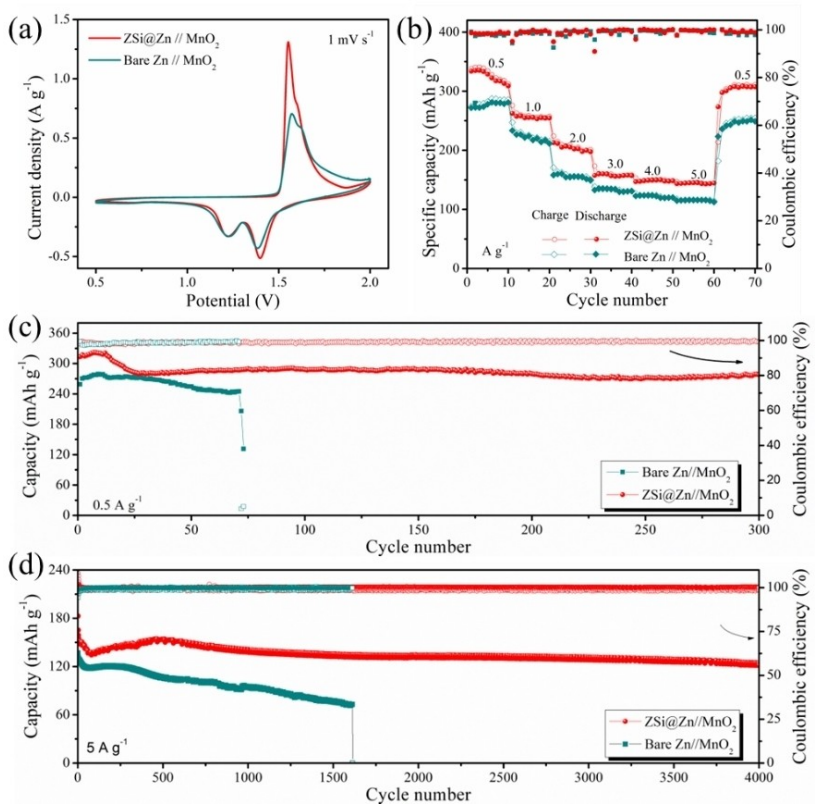


Figure 5. Electrochemical performance of Zn//MnO₂ batteries. (a) CV curves; (b) rate performance, and (c,d) cycling performance of Zn//MnO₂ with bare Zn and ZSi@Zn anodes.

the non-zincophilic interface of the bare Zn anode, which leads to significant polarization and undesirable ion migration characteristics. The ZSi@Zn//MnO₂ cell's capacity can recover to 307 mA h g⁻¹ when cycled at increased current densities and then return to 0.5 A g⁻¹. Conversely, the bare Zn//MnO₂ battery experienced rapid capacity degradation at high current densities because of the limited reversibility of bare Zn. The ZSi@Zn//MnO₂ battery exhibits a stable cycling performance with 87.2% capacity preservation and an average CE of 99.44% after 300 cycles at a current density of 0.5 A g⁻¹. This contrasts with the Zn//MnO₂ battery with bare Zn anode, which experiences electrical short-circuit failure at the 67th cycle (Figure 5c). The charge curve of the bare Zn//MnO₂ battery at 73rd cycle shows an abrupt decline in the voltage profile, which is typically indicative of a short circuit (Figure S22). Upon elevating the current density to 1 A g⁻¹ (Figure S23), an initial capacity of 226 mA h g⁻¹ is observed in ZSi@Zn//MnO₂, which maintained at 189 mA h g⁻¹ after cycling for 500 cycles. For bare Zn//MnO₂ battery, electrical shorting failure occurred after 179th cycle (Figure S22). In addition, the ZSi@Zn//MnO₂ battery remain stable for 4000 cycles and a high capacity of 122 mA h g⁻¹ can be maintained at 113 mA h g⁻¹ when cycled at a current density of 5 A g⁻¹ (Figure 5d). The swift deterioration in capacity and occurrence of electrical short-circuits in bare Zn//MnO₂ batteries can be ascribed to electrochemical corrosion and the accumulation of dendrites. These findings collectively validate the efficacy of the ZSi@Zn in enhancing the

electrochemical performance of Zn anodes by controlling deposition behavior of zinc and mitigating parasite reactions.

Conclusions

To summarize, Zn foils were treated with acidic Mercaptosilane solution, achieving simultaneous Zn(002) texture and a zinc-silane composite layer on Zn. The combined influence of these two has a remarkable synergistic impact, effectively hindering the occurrence of undesirable parasite reactions. Furthermore, this synergy actively encourages the uniform nucleation of zinc particles, contributing to a more controlled and homogeneous formation process. Additionally, it plays a pivotal role in mitigating dendrite growth, thus improving the overall stability and performance of the system. The ZSi@Zn electrodes exhibit superior electrochemical performance, with enhanced CE (99.4%) and stable cycling performance lasting over 3000 hours (1 mA cm⁻², 0.5 mA h cm⁻²). Zn//MnO₂ battery with the ZSi@Zn anode shows excellent rate capability and notably enhanced cycling stability. This work offers a simple and cost-effective method to modify Zn anodes for practical applications in aqueous zinc metal batteries.

Supporting Information

Additional references cited within the Supporting Information.^[24–26]

Acknowledgements

This work was supported by the Science Foundation for Youths of Hebei Province (No. E2021202010) and the Fund for Innovative Research Groups of Natural Science Foundation of Hebei Province (No. A2020202002).

Conflict of Interests

The authors declare no competing financial interest.

Data Availability Statement

The data that support the findings of this study are available from the corresponding author upon reasonable request.

Keywords: Zn metal anodes · Interface stability · crystal plane · dendrite-free · Zinc ion batteries

- [13] a) L. T. Kang, M. W. Cui, F. Y. Jiang, Y. F. Gao, H. J. Luo, J. J. Liu, W. Liang, C. Y. Zhi, *Adv. Energy Mater.* **2018**, *8*, 1801090; b) Y. Chu, S. Zhang, S. Wu, Z. Hu, G. Cui, J. Luo, *Energy Environ. Sci.* **2021**, *14*, 3609–3620.
- [14] J. Hao, B. Li, X. Li, X. Zeng, S. Zhang, F. Yang, S. Liu, D. Li, C. Wu, Z. Guo, *Adv. Mater.* **2020**, *32*, 2003021.
- [15] Y. Yang, C. Liu, Z. Lv, H. Yang, Y. Zhang, M. Ye, L. Chen, J. Zhao, C. C. Li, *Adv. Mater.* **2021**, *33*, e2007388.
- [16] a) P. Zou, R. Zhang, L. Yao, J. Qin, K. Kisslinger, H. Zhuang, H. L. Xin, *Adv. Energy Mater.* **2021**, *11*, 2100982; b) K. Wu, J. Yi, X. Liu, Y. Sun, J. Cui, Y. Xie, Y. Liu, Y. Xia, J. Zhang, *Nano-Micro Lett.* **2021**, *13*, 79; c) T. Chen, F. Huang, Y. N. Wang, Y. Yang, H. Tian, J. M. Xue, *Adv. Sci.* **2022**, *9*, e2105980.
- [17] a) X. C. Pu, B. Z. Jiang, X. L. Wang, W. B. Liu, L. B. Dong, F. Y. Kang, C. J. Xu, *Nano-Micro Lett.* **2020**, *12*, 152; b) H. Yang, Z. Chang, Y. Qiao, H. Deng, X. Mu, P. He, H. Zhou, *Angew. Chem. Int. Ed.* **2020**, *59*, 9377–9381.
- [18] a) H. Liu, M. Qiu, C. Tang, J. Xu, H. Jia, *Electrochim. Acta* **2022**, *405*, 139776; b) M. Qiu, H. Jia, C. Lan, H. Liu, S. Fu, *Energy Storage Mater.* **2022**, *45*, 1175–1182.
- [19] a) D. Han, S. Wu, S. Zhang, Y. Deng, C. Cui, L. Zhang, Y. Long, H. Li, Y. Tao, Z. Weng, Q.-H. Yang, F. Kang, *Small* **2020**, *16*, 2001736; b) P. F. Zhang, Z. Z. Wu, S. J. Zhang, L. Y. Liu, Y. H. Tian, Y. H. Dou, Z. Lin, S. Q. Zhang, *Nano Energy* **2022**, *102*, 107721.
- [20] H. He, H. Tong, X. Song, X. Song, J. Liu, *J. Mater. Chem. A* **2020**, *8*, 7836–7846.
- [21] W. Guo, Y. Zhang, X. Tong, X. Wang, L. Zhang, X. Xia, J. Tu, *Mater. Today Energy* **2021**, *20*, 100675.
- [22] M. Cui, Y. Xiao, L. Kang, W. Du, Y. Gao, X. Sun, Y. Zhou, X. Li, H. Li, F. Jiang, C. Zhi, *ACS Appl. Energ. Mater.* **2019**, *2*, 6490–6496.
- [23] a) Z. D. Zhao, R. Wang, C. X. Peng, W. J. Chen, T. Q. Wu, B. Hu, W. J. Weng, Y. Yao, J. X. Zeng, Z. H. Chen, P. Y. Liu, Y. C. Liu, G. S. Li, J. Guo, H. B. Lu, Z. P. Guo, *Nat. Commun.* **2021**, *12*, 6606; b) Y. Hao, D. D. Feng, L. Hou, T. Y. Li, Y. C. Jiao, P. Y. Wu, *Adv. Sci.* **2022**, *9*, e2104832.
- [24] M. Zhou, S. Guo, J. L. Li, X. B. Luo, Z. X. Liu, T. S. Zhang, X. X. Cao, M. Q. Long, B. G. Lu, A. Q. Pan, G. Z. Fang, J. Zhou, S. Q. Liang, *Adv. Mater.* **2021**, *33*, e2100187.
- [25] X. Wang, J. Meng, X. Lin, Y. Yang, S. Zhou, Y. Wang, A. Pan, *Adv. Funct. Mater.* **2021**, *31*, 2106114.
- [26] T. T. Su, K. Wang, B. Y. Chi, W. F. Ren, R. C. Sun, *Ecomat* **2022**, *4*, e12219.
- [27] F. Li, D. Ma, K. Ouyang, M. Yang, J. Qiu, J. Feng, Y. Wang, H. Mi, S. Sun, L. Sun, C. He, P. Zhang, *Adv. Energy Mater.* **2023**, *13*, 2204365.
- [28] S. Jiao, J. Fu, M. Wu, T. Hu, H. Hu, *ACS Nano* **2021**, *16*, 1013–1024.
- [29] a) J. Dong, H. Peng, J. Wang, C. Wang, D. Wang, N. Wang, W. Fan, X. Jiang, J. Yang, Y. Qian, *Energy Storage Mater.* **2023**, *54*, 875–884; b) L. Wang, Z. Wang, H. Li, D. Han, X. Li, F. Wang, J. Gao, C. Geng, Z. Zhang, C. Cui, Z. Weng, C. Yang, K. P. Loh, Q. H. Yang, *ACS Nano* **2023**, *17*, 668–677.
- [30] S. Wei, Z. H. Qi, Y. Xia, S. Chen, C. Wang, Y. Wang, P. Zhang, K. Zhu, Y. Cao, X. Guo, X. Yang, Q. Cui, X. Liu, X. Wu, L. Song, *ACS Nano* **2022**, *16*, 21152–21162.
- [31] X. Zeng, J. Mao, J. Hao, J. Liu, S. Liu, Z. Wang, Y. Wang, S. Zhang, T. Zheng, J. Liu, P. Rao, Z. Guo, *Adv. Mater.* **2021**, *33*, e2007416.
- [32] W. Li, Q. Liu, Y. Sun, J. Sun, R. Zou, G. Li, X. Hu, G. Song, G. Ma, J. Yang, Z. Chen, J. Hu, *J. Mater. Chem.* **2012**, *22*, 14864.
- [33] Z. Huang, H. Li, Z. Yang, H. Wang, J. Ding, L. Xu, Y. Tian, D. Mitlin, J. Ding, W. Hu, *Energy Storage Mater.* **2022**, *51*, 273–285.
- [34] a) S. Furukawa, N. Yamauchi, K. Nakashima, K.-I. Watanabe, H. Koda, H. Kunigami, H. Kunigami, Y. Kobayashi, *Mater. Res. Innovations* **2022**, *27*, 1–7; b) M. K. Markovic, R. Peter, I. J. Badovinac, I. Saric, M. Percic, R. Radicic, D. Markovic, M. Knez, G. Ambrozic, *Nanotechnology* **2020**, *31*, 185603.
- [35] S. Zhou, Y. Wang, H. Lu, Y. Zhang, C. Fu, I. Usman, Z. Liu, M. Feng, G. Fang, X. Cao, S. Liang, A. Pan, *Adv. Funct. Mater.* **2021**, *31*, 2104361.
- [36] Q. Li, A. Chen, D. H. Wang, Y. W. Zhao, X. Q. Wang, X. Jin, B. Xiong, C. Y. Zhi, *Nat. Commun.* **2022**, *13*, 3699.
- [37] X. Xie, S. Liang, J. Gao, S. Guo, J. Guo, C. Wang, G. Xu, X. Wu, G. Chen, J. Zhou, *Energy Environ. Sci.* **2020**, *13*, 503–510.
- [38] J. L. Yang, J. Li, J. W. Zhao, K. Liu, P. H. Yang, H. J. Fan, *Adv. Mater.* **2022**, *34*, e2202382.
- [39] a) X. Shen, X. Wang, Y. Zhou, Y. Shi, L. Zhao, H. Jin, J. Di, Q. Li, *Adv. Funct. Mater.* **2021**, *31*, 2101579; b) Z. P. Zhong, J. Y. Li, L. Y. Li, X. Y. Xi, Z. G. Luo, G. Z. Fang, S. Q. Liang, X. Y. Wang, *Energy Storage Mater.* **2022**, *46*, 165–174; c) H. Yang, W. Zhou, D. Chen, J. Liu, Z. Yuan, M. Lu, L. Shen, V. Shulga, W. Han, D. Chao, *Energy Environ. Sci.* **2022**, *15*, 1106–1118; d) S. J. Kim, D. Wu, N. Sadique, C. D. Quilty, L. Wu, A. C. Marschilok, K. J. Takeuchi, E. S. Takeuchi, Y. Zhu, *Small* **2020**, *16*, 2005406; e) V.

Soundharajan, B. Sambandam, S. Kim, S. Islam, J. Jo, S. Kim, V. Mathew, Y.-k. Sun, J. Kim, *Energy Storage Mater.* **2020**, *28*, 407–417.

Manuscript received: November 23, 2023
Revised manuscript received: December 20, 2023
Accepted manuscript online: December 25, 2023
Version of record online: January 15, 2024